MATERIALS CHEMISTRY FRONTIERS

RESEARCH ARTICLE

View Article Online
View Journal | View Issue

Cite this: *Mater. Chem. Front.*, 2023, **7**, 1411

Morphology-controllable bimetallic MOFs/textile composite electrodes with high areal capacitance for flexible electronic devices†

Shixiong Zhai,[abc] Zhendong Jin,[ab] Chengcheng Li,[ab] JiaFeng Sun,[ab] Hong Zhao,[ab] Zhehai Jin,[ab] Zaisheng Cai[ab] and Yaping Zhao *[ab]

Received 14th February 2022,
Accepted 23rd January 2023

DOI: 10.1039/d2qm00126h

rsc.li/frontiers-materials

A new strategy has been designed for enhancing the electrochemical performances of supercapacitor electrodes. In this work, flexible hetero-structure conductive cotton equipped with lamellar structure nickel/cobalt-based MOFs (NiCo-MOFs) is prepared through a self-sacrificial template method. The *in situ* conversion measure effectively strengthens the binding forces between the active materials and the current collector, which decreases the charge transfer resistance at the electrode–electrolyte interfaces. Morphological modulation of the NiCo-MOFs is carried out to construct fast transport channels for ions and charges during the charging–discharging process. The optimized NiC/NiCoMOF21 is composed of uniformly dispersed nanosheets with large gaps, which can provide more free space and active sites for electrode reactions. The energy density of the asymmetric supercapacitor (carbon cloth as the negative electrode) reaches 0.38 mW h cm^{-2} at 1.6 mW cm^{-2} (16.7% loss of the initial capacity after 2000 cycles), which overcomes the low energy storage performance of the existing textile-based electrodes.

1. Introduction

Currently, the demand for high-performance electronic devices is increasing dramatically.[1] Supercapacitors with high power density and exceptional stability have drawn extensive attention by researchers.[2,3] The electrochemical performance of supercapacitors mainly depends on the reactivity of the electrodes.[4] Therefore, optimizing the physicochemical structures of the active materials loaded on the electrodes is the key to preparing high-performance supercapacitors.[5] During the past few years, many transition metal compounds have been utilized to enhance the energy density of supercapacitors.[6] Among them, nickel (Ni) and cobalt (Co) based materials are two of the most popular materials.[7] For instance, Qian *et al.*[8] prepared a nickel sulfide (Ni_3S_2)/Ni/carbon cloth for a supercapacitor electrode, which shows a high energy density of 0.27 mW h cm^{-2} (4.90 mW cm^{-2} of the power density). Du *et al.*[9] synthesized Mo-Doped NiCoP nanoarrays that exhibited a good areal capacity of 1.99 C cm^{-2} at 2 mA cm^{-2}. Wu *et al.*[10] fabricated cobaltous hydroxide ($Co(OH)_2$)/cobaltous sulfide (Co_9S_8) nanohybrids for electrode materials. Thanks to the rich redox performance of $Co(OH)_2/Co_9S_8$, more charges could be stored in the electrodes. The specific areal capacitance of the composites reached 5.28 F cm^{-2} (2 mA cm^{-2} of the current density).

Metal–organic frameworks (MOFs), as emerging crystalline materials coordinated with organic linkers, have been regarded as promising materials for supercapacitor electrodes.[11–13] The structural properties of MOFs could optimize the molecular surface areas, which leads to the formation of a lot of chemical reaction sites.[14] Besides, the good porosity and crystallinity of MOF-based materials could enable them to supply much more charge transfer channels at electrode–electrolyte interfaces than single-phase materials.[15] Kishore *et al.*[16] reported a zinc oxide-1,4-benzene dicarbox (MOF5)/$NiCo_2O_4$ composite for supercapacitor electrodes, which exhibits a specific capacitance of 557.50 F g^{-1} at 5 mV s^{-1} of the scan rate. However, a great challenge of MOF based materials at present is their poor conductivity which resulted from the introduction of organics.[17] To solve this problem, many composite materials have been prepared. Mohanadas prepared copper-based metal–organic framework (Cu-MOF)/reduced graphene (RGO) using a hydrothermal method. Benefiting from the improved electrical conductivity, the hybrid material delivered a high specific

[a] *Key Lab of Science & Technology of Eco-textile, Ministry of Education, College of Chemistry, Chemical Engineering and Biotechnology, Donghua University, Shanghai, 201620, P. R. China. E-mail: zhaoyping@dhu.edu.cn*
[b] *College of Chemistry, Chemical Engineering and Biotechnology, Donghua University, Shanghai, 201620, P. R. China*
[c] *Department of Chemistry, University of Calgary, Calgary, Alberta, T2N 1N4, Canada*

† Electronic supplementary information (ESI) available. See DOI: https://doi.org/10.1039/d2qm00126h

energy of 31.2 W h kg^{-1} at 656.4 W kg^{-1}. Li *et al.*[18] fabricated a nickel gallium layered hydroxide nanosheet (NiGa-LDH)/carbon nanotube (CNT) composite for supercapacitor electrodes, which exhibits an improved specific capacitance of 2580 F g^{-1} at 1 A g^{-1}. Although the conductivity of MOFs has been greatly increased by combining them with highly conductive materials, most of the materials reported in the past are powders which rely on non-conductive adhesives to combine with the current collector.[19] This inevitably affects the holistic conductivity of the electrode. Therefore, directly growing MOF/highly conductive material composites on a current collector might be a feasible method to obtain high energy density electrodes with low electrical resistivity.[20]

Textiles with good flexibility and permeability could meet many practical applications.[21] It is a considerable way to combine MOFs with textiles for expanding the application scenarios of MOFs.[22] Fabric-based flexible composite materials could be used in many fields like sensors,[23] removal of oil spills,[24] ionic liquid welding,[25] photocatalysts,[26] *etc.* Cotton, as one of the most important textiles, has excellent three-dimensional interlaced network structures which could provide a large active area for active materials.[27] However, cellulose cannot be directly used for a current collector of the electrode due to its insulation properties. Many studies have been carried out to prepare a modified cotton fabric with good electrical conductivity. Ahirrao *et al.*[28] prepared a highly conductive carbon cloth (CC) through carbonizing cotton. The synthesized CC was used for flexible current collectors. The polyaniline (PANI)/CC flexible electrode showed a specific capacitance of 691 F g^{-1} at 1 A g^{-1}. Karami *et al.*[29] used RGO and silver (Ag) nanoparticles to enhance the conductivity of cotton. The symmetric supercapacitor based on Ag/RGO/cotton composite electrodes showed a large energy density of 43.2 W h Kg^{-1} at 123 W Kg^{-1}. Besides precious metals and carbon materials, Ni-based materials are also famous for preparing a cotton fabric with high electrical conductivity. Ding *et al.*[30] reported a highly conductive cotton fabric by Ni-tungsten (W)–phosphorus electroless plating for electromagnetic shielding textile. The electrical conductivity of the Ni-W-P/cotton composite was only 0.08 Ω sq^{-1}. Wang *et al.*[31] prepared NiCoS nanoflakes/cotton for a self-supporting electrode, which shows an energy density of 48.9 W h kg^{-1} at 390 W kg^{-1}. Nevertheless, conductive cotton electrodes prepared using physical or chemical methods are good candidate materials for supercapacitor electrodes. However, the low capacitive performance of the existing textile-based electrodes (TBEs) severely limited their practical application.[32] How to improve the electrochemical reactivity on TBE surfaces becomes an urgent problem.[33]

Taking into account all of the above, we attempt to equip NiCo-based MOFs on conductive cotton for preparing high-performance flexible supercapacitor electrodes (Fig. 1). In this work, conductive cotton was prepared by a electroless nickel plating method, considering that directly sacrificing a metal to provide ion sources is not conducive to the structural orientation of the products. Electrochemical oxidation was performed to enhance the interfacial properties of the Ni-plated cotton electrode. The strategy of *in situ* conversion strengthens the binding forces between the depositions and the substrate in

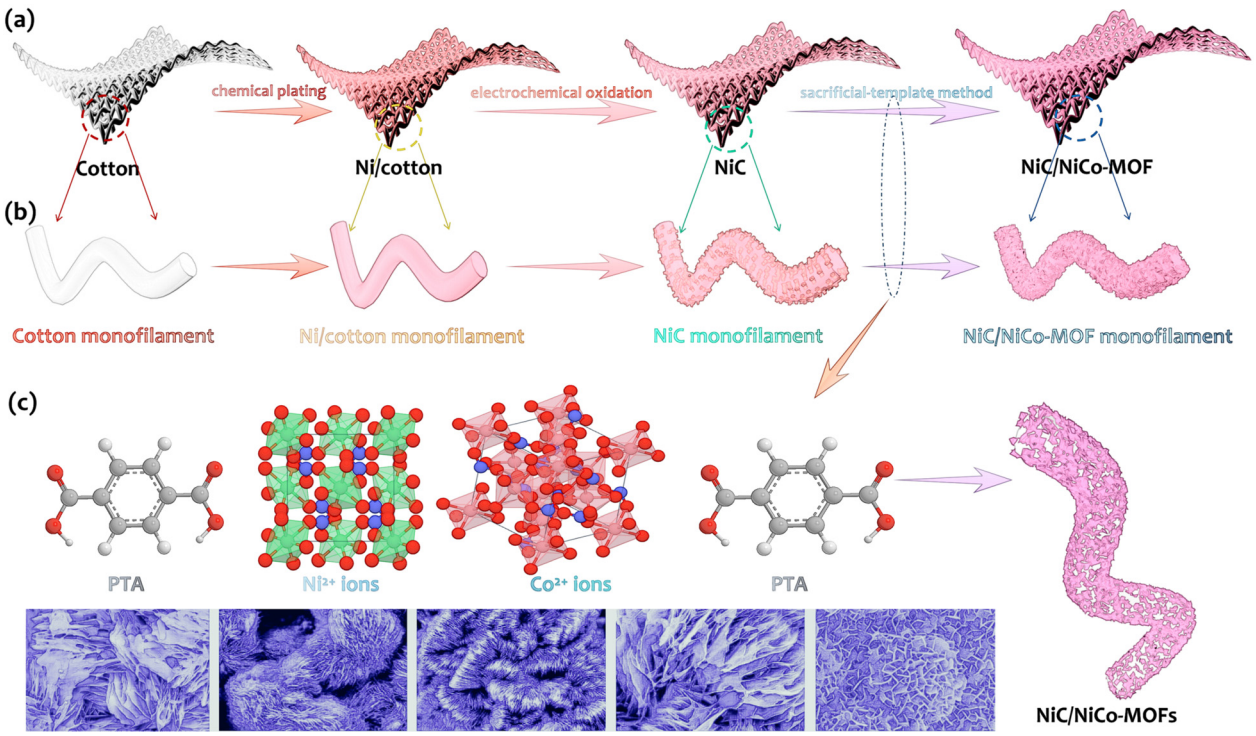

Fig. 1 Schematic diagram of the preparation process of NiC/NiCo-MOFs (a and b) and the modification process of cotton. (c) Preparation of NiC/NiCo-MOFs by a hydrothermal method.

comparison with many loose structures of Ni deposited with $Ni(OH)_2$ as previously reported.[32] Nickel nitrate ($Ni(NO_3)_2$) and cobalt nitrate ($Co(NO_3)_2$) were used as Ni and Co sources. Terephthalic acid (PTA) was used as the organic ligand. NiCo-based bimetallic MOFs were *in situ* grown on the NiC surfaces through a solvothermal method. Electron exchanges occurred between metal ions and PTA ligands under solvothermal conditions, which led to the formation of oriented MOF materials on the NiC substrate. To our knowledge, sacrificing specially structured precursor templates on a flexible substrate for synthesizing regular MOF materials has been rarely reported. The sacrifice of the template could effectively improve the actual orientation of the synthesized MOFs. We prepared NiCo-based bimetallic MOFs constructed on NiC with various compositions and morphologies by adjusting the ratio of Ni to Co. Besides, we explored the relationship between energy storage performances and physicochemical structures of the samples. The lamellar structure MOFs *in situ* grown on the NiC were combined with the Ni-microspheres firmly. These fancy three-dimensional composite structures not only reduce the electrochemical resistance of the pristine MOFs but expose numerous redox sites at the electrode–electrolyte interfaces. As we expected, the assembled supercapacitor based on the optimized NiCo-based MOF composite electrode shows a satisfactory energy density with good cycling stability. It is no doubt that exploring the construction mechanism and the structure–function relationship of NiC/NiCo-based MOFs will have a great significance for preparing high-performance supercapacitor electrodes.

2 Experiments

2.1 Materials

Cotton (220 ± 2 g m^{-2}), cobalt nitrate hexahydrate($Co(NO_3)_2{\cdot}6H_2O$), nickel nitrate hexahydrate ($Ni(NO_3)_2{\cdot}6H_2O$), terephthalic acid ($C_8H_6O_4$), *N*–*N* dimethylformamide (C_3H_7NO), nickel sulfate hexahydrate ($NiSO_4{\cdot}6H_2O$), sodium hydroxide (NaOH), potassium hydroxide (KOH), sodium citrate ($Na_3C_6H_5O_7{\cdot}2H_2O$), sodium borohydride ($NaBH_4$), and sodium hypophosphite ($NaH_2PO_2{\cdot}H_2O$) were bought from Sinopharm Chemicals (Shanghai, China). All chemicals were used directly without further purification.

2.2 Preparation of nickel-plated cotton (NiC)

Chemical plating method was used to achieve the combination of nickel (Ni) and cotton. First, cotton was treated with $NaBH_4$ (0.5 mol L^{-1}) and NaOH (0.1 mol L^{-1}) for the activation process. Second, the treated cotton was immersed into the electroless plating solution (0.1 mol L^{-1} $Ni(NO_3)_2$, 0.5 mol L^{-1} NaH_2PO_2, and 0.2 mol L^{-1} $Na_3C_6H_5O_7$) for 120 min. Third, the sample was electrochemically oxidized by cyclic polarization (0–0.6 V, 50 cycles). Platinum (Pt) wire, saturated calomel (Hg/HgO) and KOH solution (2 M) were used as the counter electrode, reference electrode and electrolyte. For convenience, the sample prepared in this step was labeled as NiC.

2.3 Preparation of the NiC/nickel cobalt metal–organic framework (NiC/NiCo-MOF)

$C_8H_6O_4$ and $Ni(NO_3)_2$ were dissolved in 18 mL of C_3H_7NO solution to form a precursor. Then, NiC was dipped in the solution for 2 h (2 mL of water was added during the ultrasonic immersing step). Third, the complex solution was transferred to a 50 mL Teflon-lined autoclave and heated at 120 °C for 120 min. A series of NiC/nickel cobalt metal–organic framework composite materials (NiC/NiCo-MOF) were obtained by adjusting the ratio of Ni^{2+} to Co^{2+}. The samples were labeled as NiC/NiCoMOF10, NiC/NiCoMOF11, NiC/NiCoMOF12, NiC/NiCoMOF21 and NiC/NiCoMOF01. NiC/NiCoMOF10 indicates that the ratio of Ni^{2+} to Co^{2+} is 1 : 0. The mass loading of the NiC/NiCo-MOFs on NiC was about 2 mg cm^{-2} (Table S1, ESI†).

2.4 Characterization

The physical structures of the samples were investigated by X-ray powder diffraction (XRD, D/max-2500PC, Cu-Kα), scanning electron microscopy (SEM, S-4800) and Fourier infrared spectroscopy (FT-IR). The chemical status of the materials was investigated by energy-dispersive X-ray spectroscopy (EDS) and X-ray photoelectron spectroscopy (XPS, 250Xi). Parameters of the theoretical calculations based on materials studio (MS) software are provided in the ESI.†

2.5 Electrochemical tests

A CHI760D electrochemical workstation was used for electrochemical testing. The samples as-prepared were directly used as working electrodes. Pt, Hg/HgO and 2 M KOH were used as the counter electrode, reference electrode and electrolyte. The electrochemical performances of the samples were determined by cyclic voltammetry (CV) and galvanostatic charge–discharge curves. The specific capacitance, energy density and power density were calculated by Formula (S1)–(S3) (ESI†). The electrical resistances of the electrodes were examined by electrochemical impedance spectroscopy (EIS, 0.01–10^5 HZ). The fabrication method of the asymmetric supercapacitor based on NiC/NiCoMOF21 and carbon cloth is given in the ESI.†

3 Results and discussion

The XRD patterns of the samples are shown in Fig. 2a and b. NiC/NiCoMOF10 shows crystalline peaks at 8.4°, 14.8°, and 16.9°, which are attributed to Ni-MOF.[34] Based on the PDF 73-1520, PDF 87-0712 and calculated XRD results (Fig. S1, ESI†), the other peaks located at 16.6°, 33.2°, 43.1° could be ascribed to (001), (100) and (111) planes of $Ni/Ni(OH)_2$. The peaks at 9.1°, 14.2° and 17.8° of NiC/NiCoMOF01 correspond to Co-MOF.[35] According to the theoretical calculation results (Fig. S1, ESI†), the characteristic peak at about 20° has not appeared, which might be ascribed to the oriented growth of the samples.[36] Both characteristic peaks of Co-MOF and Ni-MOF could be confirmed in NiC/NiCoMOF21, NiC/NiCoMOF11 and NiC/NiCoMOF12, which illustrates that the Ni^{2+} and Co^{2+} ions were

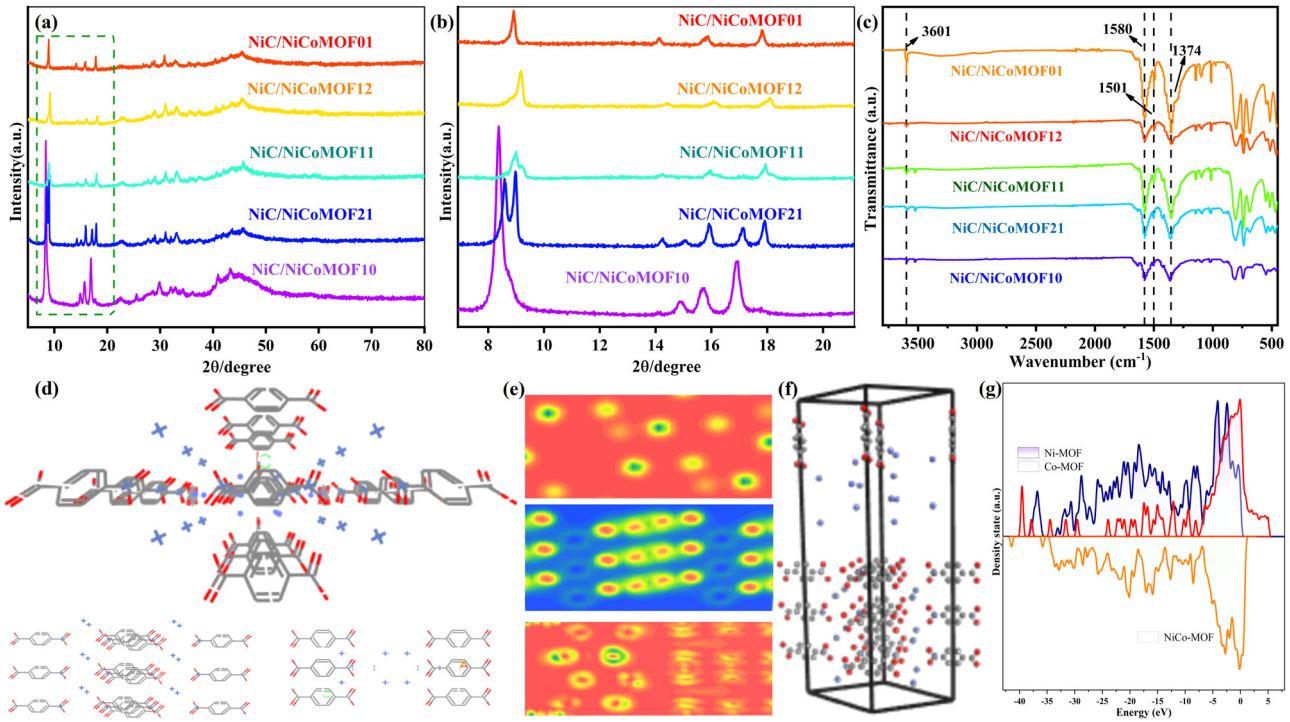

Fig. 2 (a) XRD patterns of NiC/NiCoMOFs; (b) 5–25 degree of 2θ; (c) FT-IR images; (d) molecular model of the NiCoMOF composite, Ni-MOF and Co-MOF; (e and g) electron density difference maps and total density of states; (f) binding model of Ni-MOF and Co-MOF.

well coordinated with the PTA ligands to form the MOF structure. Notably, the main peaks of Ni-MOF have not been obviously changed in NiCo-MOF composites. This could verify that the impregnation of Co^{2+} ions has no obvious effect on the crystal structure of the Ni-MOF.[35] The difference between the NiCo-MOF composites might be due to the morphology

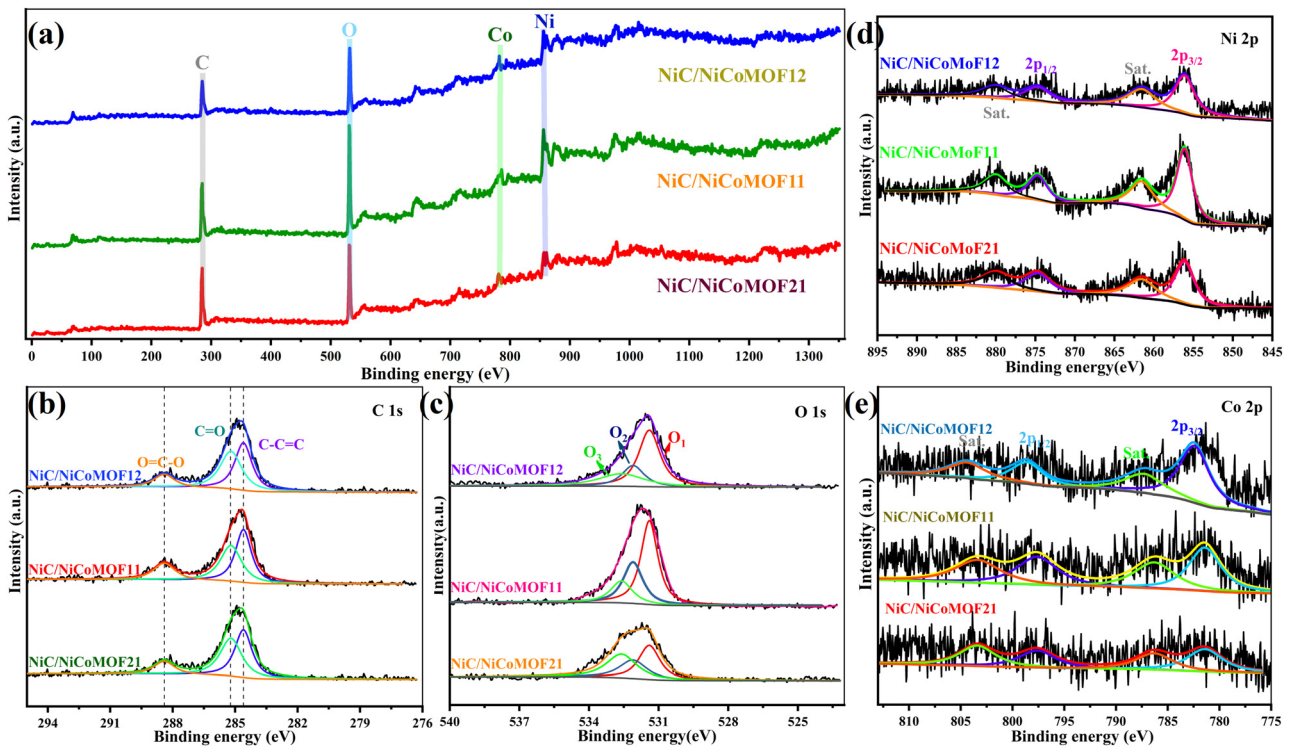

Fig. 3 XPS spectra: (a) Full survey; (b) C 1s of NiC/NiCoMOF12, NiC/NiCoMOF11, NiC/NiCoMOF21; (c) O 1s; (d and e) Ni 2p and Co 2p.

changes, which results in the anisotropy variations of the materials.[37]

Fig. 2c shows the Fourier-transform infrared (FTIR) spectra of the samples. The predominant peaks detected at about 1580 cm^{-1} and 1374 cm^{-1} could be ascribed to the –COOH groups in PTA ligands.[38] The peaks at 1501 cm^{-1} and 751 cm^{-1} are assigned to the stretching vibrations of C=C and C–H of the benzene ring.[39] Other peaks lower than 1000 cm^{-1} are attributed to Ni–OH or Co–OH groups.[40] Moreover, a distinct peak located at about 3606 cm^{-1} corresponding to benzene dicarboxylic acid coordinated with metal ions could be identified, which further confirms the structures of Co–COO–Co and Ni–COO–Ni.[41] The molecular model of NiCo-MOF is shown in Fig. 2d. Ni or Co atoms, as inorganic metal centers, bind with PTA ligands to form a crystal–organic hybrid composite with a periodic network structure. The distance between the Ni/Co atoms are significantly enlarged because of the introduction of the PTA ligand. Therefore, the difference in the charge density of Ni-MOF and Co-MOF leads to a large gap between inorganic metal atoms (Fig. 2e).[42] The total density of states (TDOS) of NiCo-MOF is calculated taking into account the DOS of both Ni-MOF and Co-MOF (Fig. 2g). The main peaks of NiCo-MOF could be well recognized as the combination of the peaks of single Ni-MOF and single Co-MOF, which demonstrates the binding stability of NiCo-MOF.[43]

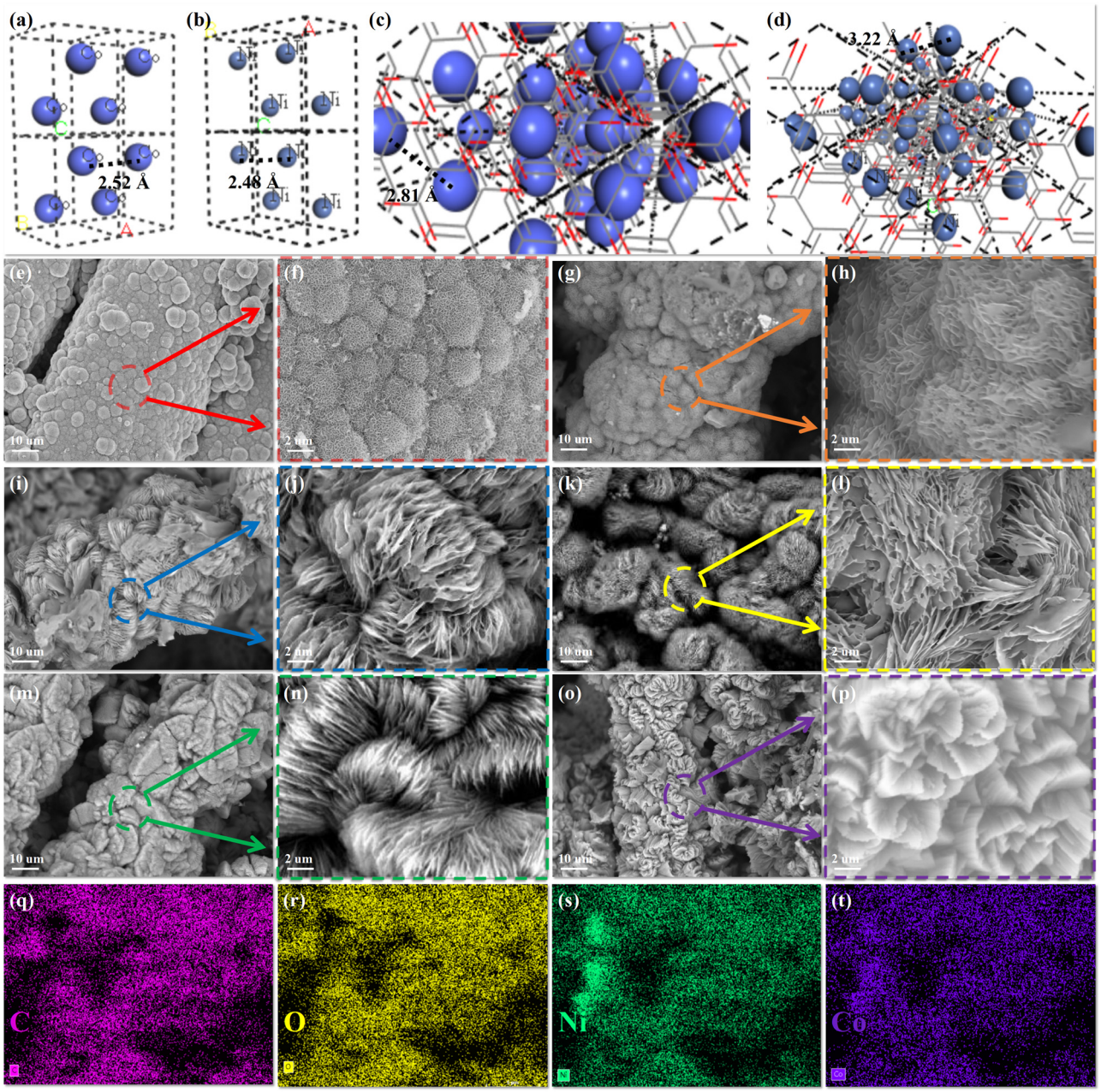

Fig. 4 (a–d) Molecular models of Co, Ni, Co-MOF and Ni-MOF; (e and f) SEM images of NiC; (g and h) NiC/NiCoMOF10; (i and j) NiC/NiCoMOF11; (k and l) NiC/NiCoMOF21; (m, n) NiC/NiCo12MOF; (o and p) NiC/NiCoMOF01. (q–t) Elemental mapping of NiC/NiCoMOF21.

The bonding states of NiC/NiCoMOF12, NiC/NiCoMOF11 and NiC/NiCo21 MOF were investigated by XPS (Fig. 3). C, O, Ni and Co elements coexist in all samples, proving the chemical composition of NiC/NiCo-MOFs (Fig. 3a). C, O and partial Ni elements are derived from the NiC substrate. The other Ni and Co elements originate from NiCo-MOFs anchored on NiC. The high-resolution spectra of C 1s, O 1s, Ni 2p and Co 2p are displayed in Fig. 3b–e. The deconvoluted peaks of C 1s at 284.6 eV, 285.2 eV and 288.7 eV correspond to C═C, C═O and O═C–O bonds (Fig. 3b).[44] Three peaks in O 1s spectra located at 531.4 eV, 532.1 eV and 532.6 eV could be observed, which are attributed to the metal–oxygen (O–Ni/Co), O–C and O═C–O bonds (Fig. 3c).[45] In Fig. 3d, the peaks at 856.1 eV and 874.7 eV are corresponding to the Ni $2p_{3/2}$ and Ni $2p_{1/2}$ in Ni^{2+}. The spin-energy separation of 17.6 eV demonstrates the existence of Ni^{2+}.[32] For Co 2p, two prominent peaks at 797.6 eV and 781.3 eV with a spin-energy separation of 16.1 eV could be assigned to Co $2p_{1/2}$ and Co $2p_{3/2}$ of Co^{2+} in NiCo-MOFs.[46] The characteristic peaks of Ni in all Ni–Co ratio samples were much more intense than those of Co. This might be due to the competitive effect of Ni^{2+} and Co^{2+} to combine with organic ligands.[47] Ni^{2+} was more likely to win the Co^{2+} in the combination process between metal ions and PTA ligands.[48]

The micro-morphologies of the samples were investigated by SEM (Fig. 4). The proportion of reactants has a huge influence on the morphology of the products. NiC/NiCo-MOFs are constructed using secondary structures with different thickness nanosheets. The distance between atoms in Fig. 4a–d was obtained from materials studio software. The distance between Co atoms (2.52 Å) is larger than that of Ni (2.48 Å), which might make Co tend to form a more stacked structure during the crystal growth process (Fig. 4a and b). Therefore, the cluster degree of the nanosheets is enhanced with the increased ratio of Co to Ni. The lattice distance of the Co-MOF (2.81 Å) and Ni-MOF (3.22 Å) is bigger than that of Co and Ni. The introduction of organic PTA could effectively separate the monatomic metals, which results in the generation of voids and a large specific surface area. The TEM and HRTEM images of NiC/NiCoMOF01 and NiC/NiCoMOF10 are shown in Fig. S5 (ESI†). The lattice distances of the two samples are 0.27 nm and 0.33 nm, which are close to the theoretical calculation values. NiC and NiC/NiCoMOF10 are micro-spheres stacked with nano-Ni flakes (Fig. 4e–l). NiC/NiCoMOF01 is composed of nano-flowers with thick nano-Co sheets. The morphologies of NiC/NiCoMOF12, NiC/NiCoMOF11 and NiC/NiCoMOF21 are accordion-like structures composed of nanosheets with different stacking degrees, which proves the occurrence of phase transformation between Ni-MOFs and Co-MOFs.[49] The distributions of NiC/NiCoMOF12 nanosheets (Fig. 4m and n) and NiC/NiCoMOF11 (Fig. 4i–g) are more disperse than NiC/NiCo-MOF01, which could provide more active sites in electrochemical reactions.[27] Compared to other samples, NiC/NiCoMOF21 has no uniformly dispersed nanosheets but large gaps between the interlaced independent units. This structure has more free

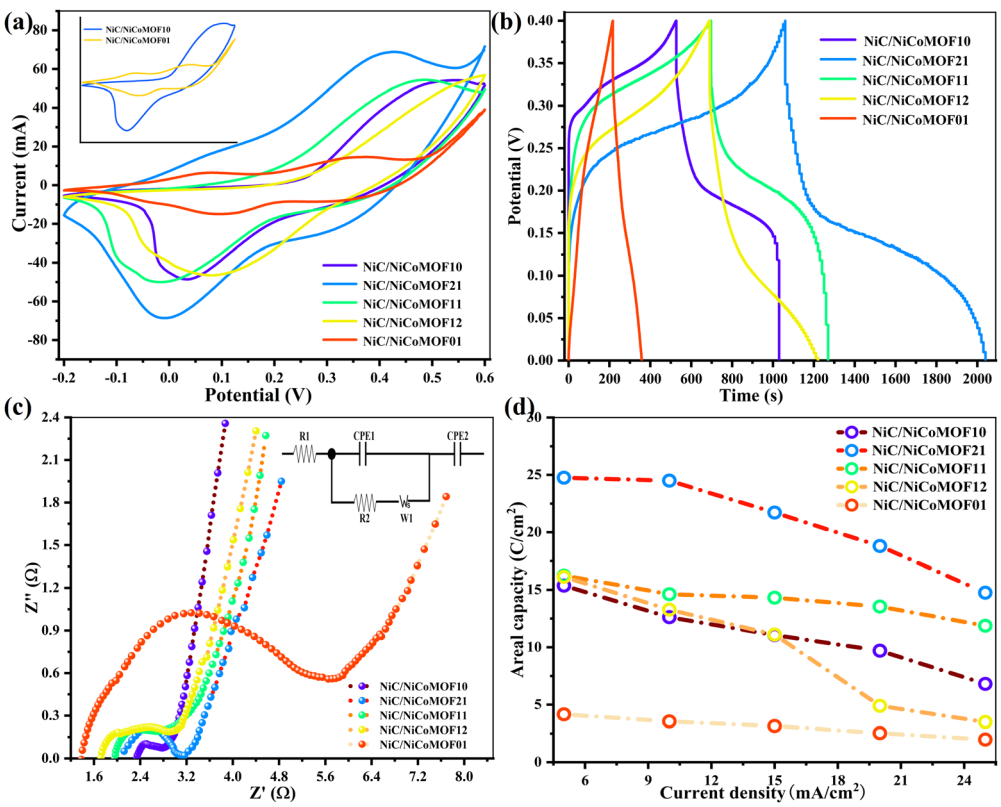

Fig. 5 (a) CV curves of the NiC/NiCo-MOFs at 5 mV s^{-1}, the inset is NiC/NiCoMOF10 and NiC/NiCoMOF01; (b) GCD curves at 10 mA cm^{-2}. (c) EIS plots (0.01 Hz to 100 kHz of the frequency range) and (d) areal capacities.

space and a favorable ion transport pathway, which is beneficial to improve the reactivity of the active material in the electrode process. Fig. 4q–t display the element mappings of the NiC/NiCoMOF21 with different magnifications compared to SEM images, which further confirms the successful coordination between Ni, Co species and organic PTA ligands.

The electrochemical performances of NiC-based NiCo-MOFs were measured using a three-electrode system. 2 M KOH aqueous solution was used as the electrolyte. Fig. 5a shows the CV curves of the five samples at 2 mV s^{-1} (−0.2 to 0.6 V of the potential window). All the samples showed similar redox peaks, which corresponds to the reversible faradaic pseudocapacitive reactions between $Ni^{2+}/Co^{2+}$and Ni^{3+}/Co^{3+}.[50] OH^- ions were intercalated and de-intercalated at the NiC/NiCoMOF-electrolyte interfaces during the electrode reaction, which results in the phase transition from Ni–O/Co–O to Ni–O–OH/Co–O–OH. NiC/NiCoMOF21 possesses the biggest CV curve area, demonstrating the optimum stoichiometric ratio of Co-MOF to Ni-MOF in NiC/NiCoMOFs. Based on Formula (S1) (ESI†), the specific capacities of the NiC/NiCoMOFs could be obtained from GCD curves (Fig. 5b and d). NiC/NiCoMOF21 shows higher specific capacity (24.4 C cm^{-2} at 10 mA cm^{-2}) than that of NiC/NiCoMOF01 (3.6 C cm^{-2} at 10 mA cm^{-2}), NiC/NiCoMOF10 (12.6 C cm^{-2} at 10 mA cm^{-2}), NiC/NiCoMOF12 (13.2 C cm^{-2} at 10 mA cm^{-2}) and NiC/NiCoMOF11 (14.6 C cm^{-2} at 10 mA cm^{-2}). The GCD curves of NiC are shown in Fig. S8 (ESI†). All the NiC/NiCoMOFs show better specific capacities than the NiC substrate (2.1 C cm^{-2}), proving the improvement in electrochemical performance by introducing the Ni-MOF and Co-MOF. Particularly, the specific capacities of all bimetallic MoFs are much higher than those of single metal-based MOFs. This suggests that synergistic effects between Ni-MOF and Co-MOF existed in the composite.[39] Interfacial reactions occurred between the two different metal-based MOFs during the hydrothermal reaction, which improves the redox reactivity of each component.[51] NiC/NiCoMOF21 has the best specific capacity among other samples, which could be ascribed to its optimized structure. N_2 adsorption–desorption isotherms of the samples are displayed in Fig. S6 (ESI†), from which it can be observed that NiC/NiCoMOF21 shows the highest specific surface (50.3 m^2 g^{-1}) area among NiC/NiCoMOF01 (27.9 m^2 g^{-1}), NiC/NiCoMOF10 (39.1 m^2 g^{-1}), NiC/NiCoMOF12 (33.4 m^2 g^{-1}) and NiC/NiCoMOF11 (43.5 m^2 g^{-1}). Two-dimensional ordered nanosheets could not only expose more available redox active sites but also shorten the ion diffusion distances, which significantly promote the reaction kinetics of the electrode. Besides, the thinner nanosheets structure of NiC/NiCoMOF21 could further improve the ion transport efficiency between the interfaces of the electrode and electrolyte.[52]

The sheet resistance of the samples was measured using a four-probe resistance tester (Table S2, ESI†). The cotton fabrics with insulating properties were changed to conductive materials after the deposition of Ni. The conductivity of the NiC/NiCoMOFs was lower than that of NiC, which might be due to the introduction of the organic PTA ligand. Furthermore, electrochemical impedance spectroscopy (EIS) was performed to study the charge transfer resistance of the samples (Fig. 5d). The intersection with real axis (Z'-axis) corresponds to the intrinsic ohmic resistance of the electrodes (R_s), and the diffusion resistance of ions is related to the diameter of the semicircle (R_{ct}). NiC/NiCoMOF01 has the lowest R_s (1.3 Ω) among NiC/NiCoMOF11 (1.98 Ω), NiC/NiCoMOF21 (2.21 Ω), NiC/NiCoMOF12 (1.69 Ω) and NiC/NiCoMOF10

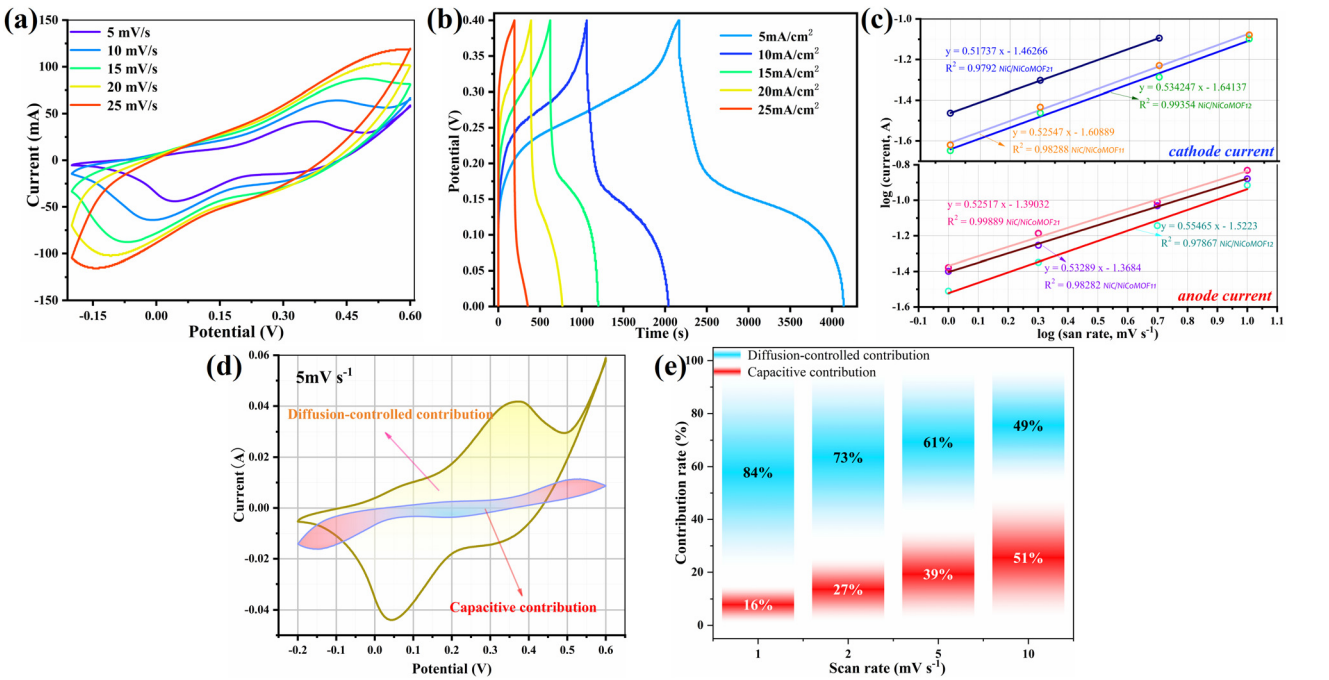

Fig. 6 CV curves of NiC/NiCoMOF21 at 5–25 mV s^{-1}. (b) GCD curves of NiC/NiCoMOF21 at 5–25 mA cm^{-2}. (c) Linear plot between log (*i*) and log (*v*) at different potentials. (d) The capacitive and diffusion-controlled contributions in the electrode process.

(2.34 Ω). This could be boiled down to the lower electrical resistivity of Co metals in comparison with the Ni metal.[53] However, NiC/NiCoMOF10 and NiC/NiCoMOF21 have lower R_{ct} values (0.7 Ω and 0.9 Ω) than NiC/NiCoMOF11 (1.0 Ω), NiC/NiCoMOF12 (1.29 Ω) and NiC/NiCoMOF01. This is because that the more dispersed nanostructures could provide numerous charge transfer channels, which accelerates the ion exchange at electrode–electrolyte interfaces.[52]

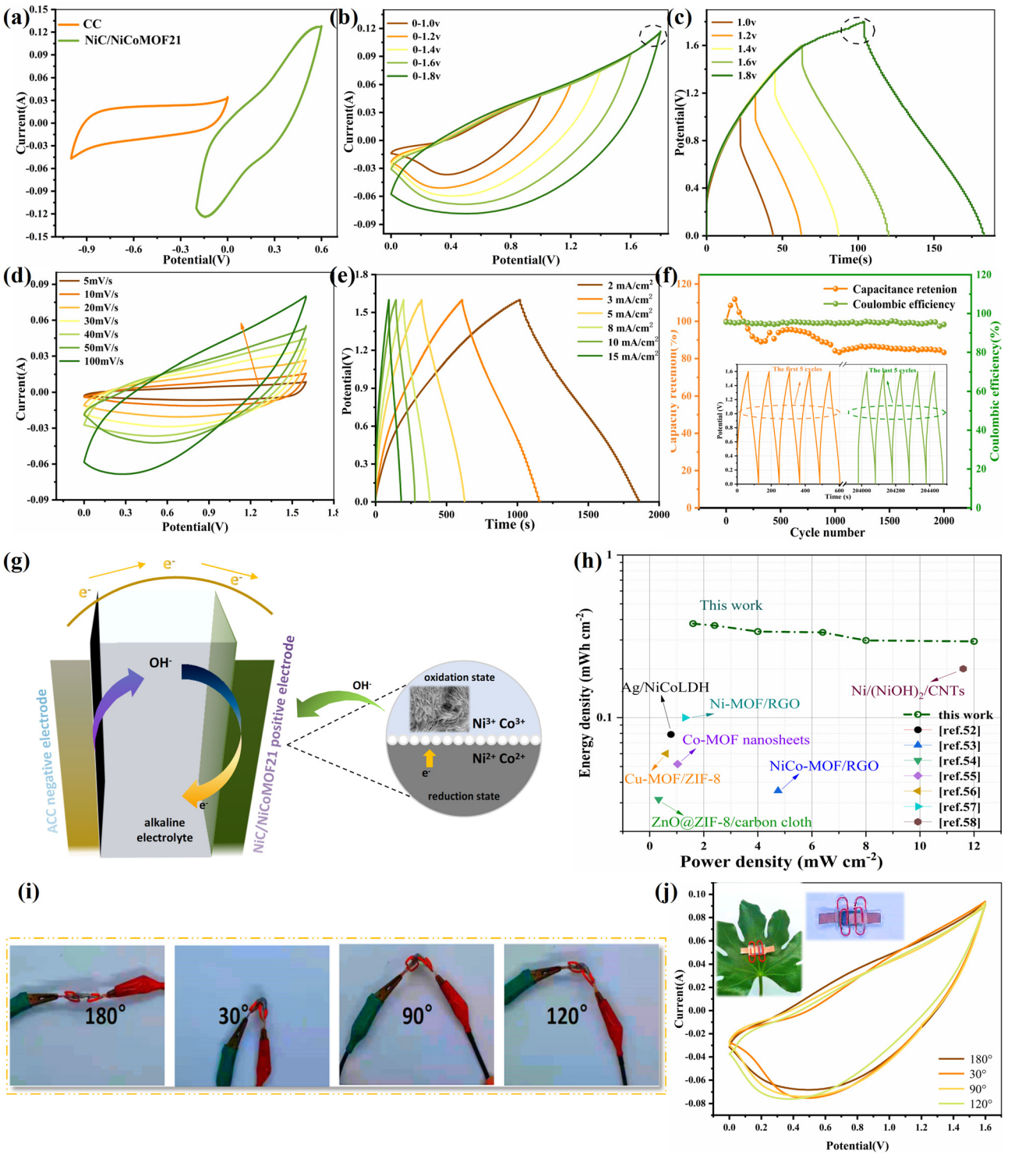

Fig. 7 (a) CV curves of NiC/NiCoMOF21 and carbon cloth at 10 mV s^{-1}; (b) CV curves of NCMC-Sp at different potential windows; (c) GCD curves; (d) CV curves of NCMC-Sp at different scan rates; (e) GCD curves of NCMC-Sp at 2–15 mA cm^{-2}; (f) cycling stability of NCMC-Sp, and the inset shows the first 5 cycles and the last 5 cycles; (g) schematic diagram of the asymmetric supercapacitor; (h) rate performance of the of the NCMC-Sp; (i and j) the CV curves at various bending angles and the inset of *j* shows the optical photograph of the NCMC-Sp.

The theory of voltammetric-response (TVR) is applied to study the charge storage kinetics of NiC/NiCoMOF21 electrodes (Formula (S4)–(S6), ESI†). The value of the electric current will be changed with the changed scan rate. In general, the logarithm of the current and the logarithm of the scan rate are linearly dependent in a surface-limited process ($i = av^1$ in Formula (S4), ESI†). If $b = 0.5$, it is a diffusion-limited reaction. The b-value could be obtained from CV curves. The b values of the NiC/NiCoMOF21 electrode are 0.52 (cathode current) and 0.53 (anode current) respectively, suggesting that the charge storage reaction of the NiC/NiCoMOF21 electrode was dominated by a diffusion-controlled process (Fig. 6a and c). The b values of NiC/NiCoMOF11 (0.53 of the cathode and anode current) and NiC/NiCoMOF12 (0.53 of the cathode current and 0.55 of the anode current) were slightly higher than those of NiC/NiCoMOF21 (Fig. 6c). This might be due to the more plentiful secondary structure supported by the stacked nanosheets of NiC/NiCoMOF21, which increase the active sites at the electrode–electrolyte interfaces. Therefore, the redox reactions of NiC/NiCoMOF21 were more sufficient, resulting in the high proportion of battery-type response in the electrode process. Based on Formula (S5) and (S6) (ESI†), the proportion of capacitive behavior ($k_1 \cdot v$) and the Faraday process ($k_2 \cdot v^{0.5}$) could be calculated. The fitting results are displayed in Fig. 6d and e. 16–51% of the total current was occupied by the surface-limited process at 1–10 mV s^{-1} of the scan rates. Diffusion-controlled contribution of the entire current became smaller at higher scan rates. This is because the redox reactions between the electrode active materials and electrolyte became insufficient at large scan rates, which makes the intercalation of OH^- ions into the electrode become more difficult. According to the Formula (S1) (ESI†), the specific capacities of NiC/NiCoMOF21 could be calculated from the GCD curves (Fig. 6b). The NiC/NiCoMOF21 electrode achieved high specific capacities of 24.8 C cm^{-2}, 24.4 C cm^{-2}, 21.7 C cm^{-2}, 18.8 C cm^{-2} and 14.6 C cm^{-2} at the current densities of 5 mA cm^{-2}, 10 mA cm^{-2}, 15 mA cm^{-2}, 20 mA cm^{-2} and 25 mA cm^{-2}. The capacity retention reached 59% with the current densities increasing from 5 to 25 mA cm^{-2}, which further indicates the excellent electrochemical energy storage performances of the NiC/NiCoMOF21.

To measure the practical performances of the NiC/NiCoMOF21 electrode, a hybrid supercapacitor (NCMC-Sp) based on NiC/NiCoMOF21 (positive electrode) and activated carbon cloth (CC, negative electrode) was assembled (Fig. 7g). The activated carbon cloth was obtained by the carbonization and KOH activation of the cotton at 800 °C under N_2 atmosphere. The suitable potential windows of Cc and NiC/NiCoMOF21 are −1 to 0 V and −0.2 to 0.6 V, demonstrating that the NCMC-Sp device is hopeful to achieve a stable voltage potential of 1.6 V (Fig. 7a). Fig. 7b shows the CV profiles of the NCA-Sp at different potential windows at 100 mV s^{-1}. The undistorted CV curves could be maintained until the voltage window was extended to 0 to 1.6 V, which confirms the matched voltage window of NCMC-Sp and Cc. Accordingly, the charges could be swimmingly stored in the electrode with a wide potential window of 1.6 V (Fig. 7c), while the polarization reaction occurred on the electrode surface made the charging process become difficult.[54] Therefore, the optimized working potential of the NCMC-Sp device is 0 to 1.6 V. The CV curves of NCMC-Sp have no obvious change at various scan rates (5–100 mV s^{-1}), suggesting the good rate performance of the device (Fig. 7d). According to Formula (S2) and S3 (ESI†) and GCD curves (Fig. 7e), the energy densities of NCMC-Sp are calculated to be 0.38, 0.36, 0.33, 0.30 and 0.29 mW h cm^{-2} at 1.6, 2.4, 4.0, 6.4, 8.0 and 12.0 mW cm^{-2}, which are comparable to those of other electrodes reported recently (Fig. 7h).[55–61] The CV curves of NCMC-Sp under different bending angles are shown in Fig. 7i and j. No obvious changes in current response curves prove the good flexibility of the NCMC-Sp. Fig. 7f shows the cycling stability of the NCMC-Sp. The capacity of the device is increased during the first 100 cycles, which could be attributed to the electrode activation process. At the beginning of the reaction, the activation of ions and the electrode active materials led to the enhancement of the electrochemical performances. As the charging and discharging process involves some irreversible redox reactions, the energy storage performance of the electrode decreased with the number of charging and discharging cycles. The performance of the supercapacitor was not changed obviously after about 1000 cycles. And 83.3% of the initial capacity with 98.4% of the coulombic efficiency could be retained after 2000 cycles, which proves the electrochemical stability of the NCMC-Sp.

4. Conclusion

In this study, a new composite electrode (NiC/NiCoMOF21) based on nickel-plated cotton and nickel/cobalt-MOF (NiCo-MOF) is prepared. The relationships between energy storage performances and physicochemical structures of the NiCo-based bimetallic MOFs are explored. Competitive effects exist between nickel ions (Ni^{2+}) and cobalt ions (Co^{2+}) during the combination process of metal ions and organic ligands. The proportion of Ni to Co in the final product is higher than the ratio of Ni^{2+} to Co^{2+} in the solution phase, which might be due to the stronger binding capacity of Ni to PTA than that of Co. The specific capacity of NiC/NiCoMOF21 with a good lamellar structure reaches 24.8, 24.4, 21.7, 18.8 and 14.6 C cm^{-2} at current densities of 5, 10, 15, 20 and 25 mA cm^{-2}. The asymmetric supercapacitor based on carbon cloth and NiC/NiCoMOF21 exhibits a high energy density of 0.38 mW h cm^{-2} at 1.6 mW cm^{-2} with good cycling stability (83.3% of the initial capacity after 2000 cycles). This work may inspire the rational design of textile-based electrode materials to achieve high performance in the field of flexible electronic devices.

Conflicts of interest

There are no conflicts to declare.

Acknowledgements

This work was funded by the Fundamental Research Funds for the Central Universities and Graduate Student Innovation Fund

of Donghua University (CUSF-DH-D-2020065), China Scholarship Council (No. 202006630075) and the National Natural Science Foundation of China (51303022).

References

1 A. Zhang, R. Zhao, L. Hu, R. Yang, S. Yao, S. Wang, Z. Yang and Y.-M. Yan, Adjusting the Coordination Environment of Mn Enhances Supercapacitor Performance of MnO2, *Adv. Energy Mater.*, 2021, **11**, 2101412.
2 R. Zhang, J. Dong, W. Zhang, L. Ma, Z. Jiang, J. Wang and Y. Huang, Synergistically coupling of 3D FeNi-LDH arrays with Ti3C2Tx-MXene nanosheets toward superior symmetric supercapacitor, *Nano Energy*, 2022, **91**, 106633.
3 Y. Zhang, W. Wang, L. Wang, Q. Guo, H. Hu, C. Xie, J. Shang, J. Xu, Y. Zhang and Z. Zheng, Inverse Opaline Metallic Membrane Addresses the Tradeoff Between Volumetric Capacitance and Areal Capacitance of Supercapacitor, *Adv. Energy Mater.*, 2022, **12**, 2102802.
4 B. K. Deka, A. Hazarika, M.-J. Kwak, D. C. Kim, A. P. Jaiswal, H. G. Lee, J. Seo, C. Jeong, J.-H. Jang, Y.-B. Park and H. W. Park, Triboelectric nanogenerator-integrated structural supercapacitor with in situ MXene-dispersed N-doped Zn–Cu selenide nanostructured woven carbon fiber for energy harvesting and storage, *Energy Storage Mater.*, 2021, **43**, 402–410.
5 X. Jin, L. Song, H. Yang, C. Dai, Y. Xiao, X. Zhang, Y. Han, C. Bai, B. Lu, Q. Liu, Y. Zhao, J. Zhang, Z. Zhang and L. Qu, Stretchable supercapacitor at −30 °C, *Energy Environ. Sci.*, 2021, **14**, 3075–3085.
6 Y. Dahiya, M. Hariram, M. Kumar, A. Jain and D. Sarkar, Modified transition metal chalcogenides for high performance supercapacitors: Current trends and emerging opportunities, *Coord. Chem. Rev.*, 2022, **451**, 214265.
7 K. Ren, Z. Liu, T. Wei and Z. Fan, Recent Developments of Transition Metal Compounds-Carbon Hybrid Electrodes for High Energy/Power Supercapacitors, *Nano-Micro Lett.*, 2021, **13**, 129.
8 H. Qian, B. Wu, Z. Nie, T. Liu, P. Liu, H. He, J. Wu, Z. Chen and S. Chen, A flexible Ni3S2/Ni@CC electrode for high-performance battery-like supercapacitor and efficient oxygen evolution reaction, *Chem. Eng. J.*, 2021, **420**, 127646.
9 W. Du, Q. Zong, J. Zhan, H. Yang and Q. Zhang, Tailoring Mo-Doped NiCoP Grown on (Ni,Co)Se2 Nanoarrays for Asymmetric Supercapacitor with Enhanced Electrochemical Performance, *ACS Appl. Energy Mater.*, 2021, **4**, 6667–6677.
10 B. Wu, F. Zhang, Z. Nie, H. Qian, P. Liu, H. He, J. Wu, Z. Chen and S. Chen, A high-performance battery-like supercapacitor electrode with a continuous NiTe network skeleton running throughout Co(OH)2/Co9S8 nanohybrid, *Electrochim. Acta*, 2021, **365**, 137325.
11 H. Zhang, B. Yan, C. Zhou, J. Wang, H. Duan, D. Zhang and H. Zhao, MOF-Derived Hollow and Porous Co3O4 Nanocages for Superior Hybrid Supercapacitor Electrodes, *Energy Fuels*, 2021, **35**, 16925–16932.
12 J. Chu, Y. Wang, F. Zhong, X. Feng, W. Chen, X. Ai, H. Yang and Y. Cao, Metal/covalent-organic frameworks for electrochemical energy storage applications, *EcoMat*, 2021, **3**, e12133.
13 B. Chen, L. Xu, Z. Xie and W.-Y. Wong, Supercapacitor electrodes based on metal-organic compounds from the first transition metal series, *EcoMat*, 2021, **3**, e12106.
14 L.-D. Ye, F. Rouhani, H. Kaviani, Q. Miao, X.-Q. Cai, A. Morsali and M.-L. Hu, Effect of Proton Conduction on the Charge Storage Mechanism of a MOF as a Supercapacitor Electrode, *J. Phys. Chem. C*, 2021, **125**, 22951–22959.
15 Z. Ma, R. Zheng, Y. Liu, Y. Ying and W. Shi, Carbon nanotubes interpenetrating MOFs-derived Co-Ni-S composite spheres with interconnected architecture for high performance hybrid supercapacitor, *J. Colloid Interface Sci.*, 2021, **602**, 627–635.
16 S. Kishore, babu, M. Jayachandran, T. Maiyalagan, T. Vijayakumar and B. Gunasekaran, Metal-organic framework (MOF-5) incorporated on NiCo2O4 as electrode material for supercapacitor application, *Mater. Lett.*, 2021, **302**, 130338.
17 L. Cheng, Q. Zhang, M. Xu, Q. Zhai and C. Zhang, Two-for-one strategy: Three-dimensional porous Fe-doped Co3O4 cathode and N-doped carbon anode derived from a single bimetallic metal-organic framework for enhanced hybrid supercapacitor, *J. Colloid Interface Sci.*, 2021, **583**, 299–309.
18 C. Li, G. Zhang, X. Li, H. Wang, P. Huo, Y. Yan and X. Wang, Construction of hierarchical layered hydroxide grown in situ on carbon tubes derived from a metal-organic framework for asymmetric supercapacitors, *Dalton Trans.*, 2021, **50**, 7337–7347.
19 M. Zeeshan and M. Shahid, State of the art developments and prospects of metal–organic frameworks for energy applications, *Dalton Trans.*, 2022, **51**, 1675–1723.
20 S. Zhai, Y. Luo, Z. Fan, M. Zhou, K. Hou, H. Zhao, M. Hu, Y. Xiao, K. Jin, Y. Zhao, X. Li and Z. Cai, Porous carbonized cotton loaded with Zn–Cu–M(M = O, S) nanocomposites for electrochemical energy storage and oxygen evolution reaction, *Mater. Today Energy*, 2021, **21**, 100806.
21 S. Zhai, Y. Li, W. Dong, H. Zhao, K. Ma, H. Zhang, H. Wang, Y. Zhao, X. Li and Z. Cai, Cationic cotton modified by 3-chloro-2-hydroxypropyl trimethyl ammonium chloride for salt-free dyeing with high levelling performance, *Cellulose*, 2022, **29**, 633–646.
22 A. Yang, Z. Wang and Y. Zhu, Facile preparation and adsorption performance of low-cost MOF@cotton fibre composite for uranium removal, *Sci. Rep.*, 2020, **10**, 19271.
23 J. Song, M. Huang, X. Lin, S. F. Y. Li, N. Jiang, Y. Liu, H. Guo and Y. Li, Novel Fe-based metal–organic framework (MOF) modified carbon nanofiber as a highly selective and sensitive electrochemical sensor for tetracycline detection, *Chem. Eng. J.*, 2022, **427**, 130913.
24 R. Dalapati, S. Nandi, C. Gogoi, A. Shome and S. Biswas, Metal–Organic Framework (MOF) Derived Recyclable, Superhydrophobic Composite of Cotton Fabrics for the Facile Removal of Oil Spills, *ACS Appl. Mater. Interfaces*, 2021, **13**, 8563–8573.
25 M. A. Bunge, E. Pasciak, J. Choi, L. Haverhals, W. M. Reichert and T. G. Glover, Ionic Liquid Welding of the

UIO-66-NH2 MOF to Cotton Textiles, *Ind. Eng. Chem. Res.*, 2020, **59**, 19285–19298.

26 H. E. Emam, H. B. Ahmed, E. Gomaa, M. H. Helal and R. M. Abdelhameed, Recyclable photocatalyst composites based on Ag3VO4 and Ag2WO4 @MOF@cotton for effective discoloration of dye in visible light, *Cellulose*, 2020, **27**, 7139–7155.

27 S. Zhai, K. Jin, M. Zhou, Z. Fan, H. Zhao, Y. Zhao, X. Li and Z. Cai, In-situ growth of flower-like CuS microsphere on carbonized cotton for high-performance flexible supercapacitor, *Colloids Surf., A*, 2019, **575**, 75–83.

28 D. J. Ahirrao, A. K. Pal, V. Singh and N. Jha, Nanostructured porous polyaniline (PANI) coated carbon cloth (CC) as electrodes for flexible supercapacitor device, *J. Mater. Sci. Technol.*, 2021, **88**, 168–182.

29 Z. Karami, M. Youssefi, K. Raeissi and M. Zhiani, Effect of the morphology of silver layer on electrical conductivity and electrochemical performance of silver/reduced graphene oxide/cotton fabric composite as a flexible supercapacitor electrode, *J. Energy Storage*, 2021, **42**, 103042.

30 X. Ding, W. Wang, Y. Wang, R. Xu and D. Yu, High-performance flexible electromagnetic shielding polyimide fabric prepared by nickel-tungsten-phosphorus electroless plating, *J. Alloys Compd.*, 2019, **777**, 1265–1273.

31 Z. Wang, H. Wang, S. Ji, H. Wang, D. J. L. Brett and R. Wang, Design and synthesis of tremella-like Ni–Co–S flakes on co-coated cotton textile as high-performance electrode for flexible supercapacitor, *J. Alloys Compd.*, 2020, **814**, 151789.

32 Z. Jin, M. Zhou, J. Hu, K. Li, L. Tang, H. Zhao, Z. Cai and Y. Zhao, Hierarchical Ni@Ni(OH)2 core-shell hybrid arrays on cotton cloth fabricated by a top-down approach for high-performance flexible asymmetric supercapacitors, *J. Alloys Compd.*, 2019, **784**, 1091–1098.

33 S. Zhai, K. Jin, M. Zhou, Z. Fan, H. Zhao, X. Li, Y. Zhao, F. Ge and Z. Cai, A novel high performance flexible supercapacitor based on porous carbonized cotton/ZnO nanoparticle/CuS micro-sphere, *Colloids Surf., A*, 2020, **584**, 124025.

34 M.-Y. Zong, C.-Z. Fan, X.-F. Yang and D.-H. Wang, Promoting Ni-MOF with metallic Ni for highly-efficient p-nitrophenol hydrogenation, *Mol. Catal.*, 2021, **509**, 111609.

35 J.-C. Wang, F.-W. Ding, J.-P. Ma, Q.-K. Liu, J.-Y. Cheng and Y.-B. Dong, Co(II)-MOF: A Highly Efficient Organic Oxidation Catalyst with Open Metal Sites, *Inorg. Chem.*, 2015, **54**, 10865–10872.

36 H. Sun, M. Dong, Z. Peng, H. Wang, D. Zhang, Q. Wang, Z. Hu, Z. Li and B. Wang, Unveiling the key factors affecting the grain size of NiCo2O4 during electrodeposition, *Appl. Surf. Sci.*, 2022, **606**, 154899.

37 D. Huang, L. Chen, L. Yue, F. Yang, H. Guo and W. Yang, Nitrogen-doped carbon-enriched MOF and derived hierarchical carbons as electrode for excellent asymmetric aqueous supercapacitor, *J. Alloys Compd.*, 2021, **867**, 158764.

38 Z.-J. Lin, H.-Q. Zheng, J. Chen, W.-E. Zhuang, Y.-X. Lin, J.-W. Su, Y.-B. Huang and R. Cao, Encapsulation of Phosphotungstic Acid into Metal–Organic Frameworks with Tunable Window Sizes: Screening of PTA@MOF Catalysts for Efficient Oxidative Desulfurization, *Inorg. Chem.*, 2018, **57**, 13009–13019.

39 Y. Wang, Y. Liu, H. Wang, W. Liu, Y. Li, J. Zhang, H. Hou and J. Yang, Ultrathin NiCo-MOF Nanosheets for High-Performance Supercapacitor Electrodes, *ACS Appl. Energy Mater.*, 2019, **2**, 2063–2071.

40 Y. Du, G. Li, M. Chen, X. Yang, L. Ye, X. Liu and L. Zhao, Hollow nickel-cobalt-manganese hydroxide polyhedra via MOF templates for high-performance quasi-solid-state supercapacitor, *Chem. Eng. J.*, 2019, **378**, 122210.

41 P. Thangasamy, S. Shanmuganathan and V. Subramanian, A NiCo-MOF nanosheet array based electrocatalyst for the oxygen evolution reaction, *Nanoscale Adv.*, 2020, **2**, 2073–2079.

42 K. Zhu, R. Fan, J. Wu, B. Wang, H. Lu, X. Zheng, T. Sun, S. Gai, X. Zhou and Y. Yang, MOF-on-MOF Membrane with Cascading Functionality for Capturing Dichromate Ions and p-Arsanilic Acid Turn-On Sensing, *ACS Appl. Mater. Interfaces*, 2020, **12**, 58239–58251.

43 X. Han, D. Zhang, Y. Qin, X. Kong, F. Zhang and X. Lei, Construction of Ta-Cu7S4 negative electrode for high-performance all-solid-state asymmetric supercapacitor, *Chem. Eng. J.*, 2021, **403**, 126471.

44 S. Gao, X. Wang, C. Song, S. Zhou, F. Yang and Y. Kong, Engineering carbon-defects on ultrathin g-C3N4 allows one-pot output and dramatically boosts photoredox catalytic activity, *Appl. Catal., B*, 2021, **295**, 120272.

45 Y. Liu, Y. Wang, H. Wang, P. Zhao, H. Hou and L. Guo, Acetylene black enhancing the electrochemical performance of NiCo-MOF nanosheets for supercapacitor electrodes, *Appl. Surf. Sci.*, 2019, **492**, 455–463.

46 J. Li, Y. Deng, L. Leng, M. Liu, L. Huang, X. Tian, H. Song, X. Lu and S. Liao, MOF-Templated sword-like Co3O4@Ni-Co2O4 sheet arrays on carbon cloth as highly efficient Li–O2 battery cathode, *J. Power Sources*, 2020, **450**, 227725.

47 X. Hang, Y. Xue, Y. Cheng, M. Du, L. Du and H. Pang, From Co-MOF to CoNi-MOF to Ni-MOF: A Facile Synthesis of 1D Micro-/Nanomaterials, *Inorg. Chem.*, 2021, **60**, 13168–13176.

48 F. U. Zuhri, M. Diantoro, L. Suryanti and T. Suprayogi, Nasikhudin, Sunaryono and W. Meevasana, ZnO-FC-NiCo MOF for prospective supercapacitor materials, *Mater. Today: Proc.*, 2021, **44**, 3385–3389.

49 Z. Chen, Y. Ha, H. Jia, X. Yan, M. Chen, M. Liu and R. Wu, Oriented Transformation of Co-LDH into 2D/3D ZIF-67 to Achieve Co–N–C Hybrids for Efficient Overall Water Splitting, *Adv. Energy Mater.*, 2019, **9**, 1803918.

50 Y. Zheng, S. Zheng, Y. Xu, H. Xue, C. Liu and H. Pang, Ultrathin two-dimensional cobalt-organic frameworks nanosheets for electrochemical energy storage, *Chem. Eng. J.*, 2019, **373**, 1319–1328.

51 X. Shi, L. Sun, X. Li, L. Wu, J. Qian, J. Wang, Y. Lin, S. Su, C. Sun, Y. Zhang and Y. Zhang, High-performance flexible supercapacitor enabled by Polypyrrole-coated NiCoP@CNT electrode for wearable devices, *J. Colloid Interface Sci.*, 2022, **606**, 135–147.

52 C. Hao, X. Wang, X. Wu, Y. Guo, L. Zhu and X. Wang, Composite material CCO/Co-Ni-Mn LDH made from sacrifice template CCO/ZIF-67 for high-performance supercapacitor, *Appl. Surf. Sci.*, 2022, **572**, 151373.

53 Q. Yang, Y. Liu, M. Yan, Y. Lei and W. Shi, MOF-derived hierarchical nanosheet arrays constructed by interconnected NiCo-alloy@NiCo-sulfide core-shell nanoparticles for high-performance asymmetric supercapacitors, *Chem. Eng. J.*, 2019, **370**, 666–676.

54 M. Gao, Y. Li, J. Yang, Y. Liu, Y. Liu, X. Zhang, S. Wu and K. Cai, Nickel-cobalt (oxy)hydroxide battery-type supercapacitor electrode with high mass loading, *Chem. Eng. J.*, 2022, **429**, 132423.

55 S. C. Sekhar, G. Nagaraju and J. S. Yu, Conductive silver nanowires-fenced carbon cloth fibers-supported layered double hydroxide nanosheets as a flexible and binder-free electrode for high-performance asymmetric supercapacitors, *Nano Energy*, 2017, **36**, 58–67.

56 J. Cheng, S. Chen, D. Chen, L. Dong, J. Wang, T. Zhang, T. Jiao, B. Liu, H. Wang, J.-J. Kai, D. Zhang, G. Zheng, L. Zhi, F. Kang and W. Zhang, Editable asymmetric all-solid-state supercapacitors based on high-strength, flexible, and programmable 2D-metal–organic framework/reduced graphene oxide self-assembled papers, *J. Mater. Chem. A*, 2018, **6**, 20254–20266.

57 X.-M. Cao and Z.-B. Han, Hollow core–shell ZnO@ZIF-8 on carbon cloth for flexible supercapacitors with ultrahigh areal capacitance, *Chem. Commun.*, 2019, **55**, 1746–1749.

58 S. Dai, F. Han, J. Tang and W. Tang, MOF-derived Co3O4 nanosheets rich in oxygen vacancies for efficient all-solid-state symmetric supercapacitors, *Electrochim. Acta*, 2019, **328**, 135103.

59 D. Nagaraju, D. G. Bhagat, R. Banerjee and U. K. Kharul, In situ growth of metal-organic frameworks on a porous ultrafiltration membrane for gas separation, *J. Mater. Chem. A*, 2013, **1**, 8828–8835.

60 C. Cheng, J. Xu, W. Gao, S. Jiang and R. Guo, Preparation of flexible supercapacitor with RGO/Ni-MOF film on Ni-coated polyester fabric, *Electrochim. Acta*, 2019, **318**, 23–31.

61 S. Zhai, M. Li, Z. Jin, J. Sun, H. Zhao, Z. Cai and Y. Zhao, The fabrication of flexible wearable electrodes based on a carbon nanotubes/nickel/nickelous hydroxide ternary composite by facile single-side printing technology, *Dalton Trans.*, 2021, **50**, 12860–12869.

